J. Fluid Mech. (2019), *vol.* 865, R2, doi:10.1017/jfm.2019.132

JFM RAPIDS
journals.cambridge.org/rapids

Stability of the Prandtl model for katabatic slope flows

Cheng-Nian Xiao and Inanc Senocak†

Department of Mechanical Engineering and Materials Science, University of Pittsburgh, Pittsburgh, PA 15261, USA

(Received 2 December 2018; revised 5 February 2019; accepted 7 February 2019; first published online 28 February 2019)

We investigate the stability of the Prandtl model for katabatic slope flows using both linear stability theory and direct numerical simulations. Starting from Prandtl's analytical solution for uniformly cooled laminar slope flows, we use linear stability theory to identify the onset of instability and features of the most unstable modes. Our results show that the Prandtl model for parallel katabatic slope flows is prone to transverse and longitudinal modes of instability. The transverse mode of instability manifests itself as stationary vortical flow structures aligned in the along-slope direction, whereas the longitudinal mode of instability emerges as waves propagating in the base-flow direction. Beyond the stability limits, these two modes of instability coexist and form a complex flow structure crisscrossing the plane of flow. The emergence of a particular form of these instabilities depends strongly on three dimensionless parameters, which are the slope angle, the Prandtl number and a newly introduced stratification perturbation parameter, which is proportional to the relative importance of the disturbance to the background stratification due to the imposed surface buoyancy flux. We demonstrate that when this parameter is sufficiently large, then the stabilising effect of the background stratification can be overcome. For shallow slopes, the transverse mode of instability emerges despite meeting the Miles–Howard stability criterion of $Ri > 0.25$. At steep slope angles, slope flow can remain linearly stable despite attaining Richardson numbers as low as 3×10^{-3}.

Key words: atmospheric flows, stratified flows

1. Introduction

Katabatic slope flows are gravity-driven winds that are common over continental-scale ice sheets or over snow-covered mountainous terrain where cold air flows downhill. Katabatic winds play a vital role in reliable weather predictions pertaining to air quality, aviation and agriculture. A landmark study in understanding of katabatic

---

† Email address for correspondence: senocak@pitt.edu

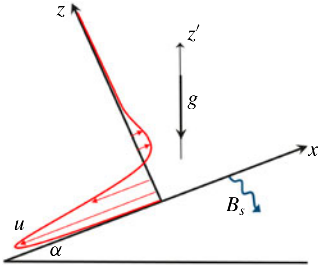

FIGURE 1. Sketch of the slope flow and the rotated coordinate system.

winds is that of Prandtl (1942), in which an analytical solution was developed for a viscous stably stratified quiescent fluid over an infinitely long and uniformly cooled planar surface with a constant slope to it. Despite its simplicity, Prandtl's solution exhibits the vertical structure of katabatic winds observed in nature. The buoyancy and velocity profile predicted by Prandtl's laminar flow solution is an exponentially dampened sinusoidal wave with growing height (Fedorovich & Shapiro 2009). The solution produces a low-level strong jet along the slope descent, which is capped by a weak reverse flow, as depicted in figure 1.

Despite its usefulness in explaining katabatic slope flows, the linear stability of the Prandtl model and the parameter space in which the underlying assumptions hold have not been investigated in the open literature. Fedorovich & Shapiro (2009) introduced an integral slope flow Reynolds number, Re_I, that is a function of the slope angle, Brunt–Väisälä frequency, surface buoyancy flux and the kinematic viscosity. They performed direct numerical simulation (DNS) of fully developed turbulence with Re_I ranging from 3000 to 10 000. Umphrey, DeLeon & Senocak (2017) adopted the same definition of the Reynolds numbers and conducted laminar katabatic flow computations for $Re_I = 20$ to validate and verify a Navier–Stokes solver. In Shapiro & Fedorovich (2014), it was hypothesised that katabatic slope flows are governed by two independent dimensionless parameters, namely Reynolds and Prandtl numbers. The slope angle appeared as a stretching factor in their Reynolds number definition because Shapiro & Fedorovich worked with boundary-layer approximated equations. As we show in the next section, linear stability of the Prandtl model strongly depends on three non-dimensional parameters, which are the slope angle, the Prandtl number, and a new dimensionless parameter that we introduce in § 3.

Recently, a number of numerical and experimental studies have been devoted to study instabilities in stably stratified fluid cases. Facchini *et al.* (2018) investigated linear instability of Couette flow with stable stratification via both experiments and DNS, whereas Chen, Bai & Le Dizès (2016) studied stably stratified horizontal boundary layers on a vertical wall; in both cases, the direction of stratification was orthogonal to both the shear and base-flow directions. The case where the direction of stratification was orthogonal to the base-flow direction but makes an angle with the plane of shear was analysed by Candelier, Le Dizès & Le Dizès (2011), who identified inviscid instabilities generated by a Bickley jet ejected onto a sloping surface. The Prandtl model for slope flows is uniquely different from these cases as the direction of stratification is oblique to both the base-flow direction and the direction of shear due to the inclination of the surface. In the aforementioned studies, linear stability analysis (LSA) has been used to identify the stability limits. Here, we follow the same general strategy to identify the instabilities and conduct DNS to support the findings of the LSA and visualise the nature of flow instabilities.

2. Governing equations

The idealised slope flow configuration is shown in figure 1, where α is the constant slope angle and gravity acts in the vertical direction. B_s is the constant heat flux imposed on the surface. For ease of analysis, the problem is studied in a rotated Cartesian coordinate system whose x axis is aligned with the planar inclined surface. Let u be the along-slope (longitudinal), v be the cross-slope (transverse), and w be the slope-normal velocity components, such that $u_i = [u, v, w]$ is the velocity vector. The gravity vector in the rotated coordinate system is then given by $g_i = [g_1, g_2, g_3] = [\sin\alpha, 0, \cos\alpha]$. The buoyancy and the Brunt–Väisälä frequency are denoted by b, N, respectively, where N^2 is used as a measure of stratification. Following the presentation in Fedorovich & Shapiro (2009), the momentum and the buoyancy balance equations with a Boussinesq approximation are written as follows:

$$\frac{\partial u_i}{\partial t} + \frac{\partial u_i u_j}{\partial x_j} = -\frac{1}{\rho}\frac{\partial p}{\partial x_i} + \frac{\partial}{\partial x_j}\left(\nu \frac{\partial u_i}{\partial x_j}\right) + b g_i, \tag{2.1}$$

$$\frac{\partial b}{\partial t} + \frac{\partial b u_j}{\partial x_j} = \frac{\partial}{\partial x_j}\left(\beta \frac{\partial b}{\partial x_j}\right) - N^2 g_j u_j, \tag{2.2}$$

where ν, β are the kinematic viscosity and thermal diffusivity of the fluid, respectively. The conservation of mass principle is imposed by a divergence-free velocity field

$$\frac{\partial u_i}{\partial x_i} = 0. \tag{2.3}$$

In the following, the position and velocity vector components x_i, u_i are denoted as $[x, y, z]^{\mathrm{T}}$ and $[u, v, w]^{\mathrm{T}}$, respectively. Buoyancy is related to the potential temperature as $b = g\theta/\Theta_r$, where Θ_r is a reference potential temperature value. At the surface, a negative buoyancy flux B_s is imposed to create katabatic flow conditions.

In the Prandtl model, equation (2.1) reduces to a balance between buoyancy and diffusion of along-slope momentum; and (2.2) reduces to a balance between along-slope momentum and diffusion of buoyancy. For the case with a constant buoyancy flux at the surface, Shapiro & Fedorovich (2004) provides the following one-dimensional exact solution:

$$u_n = \sqrt{2}\sin(z_n/\sqrt{2})\exp(-z_n/\sqrt{2}), \tag{2.4}$$

$$b_n = \sqrt{2}\cos(z_n/\sqrt{2})\exp(-z_n/\sqrt{2}), \tag{2.5}$$

where $z_n = z/l_0$, $u_n = u/u_0$, $b_n = b/b_0$ are non-dimensional height, velocity, and buoyancy, respectively, and the corresponding scales governing the flow problem are given as (Fedorovich & Shapiro 2009)

$$l_0 = (\nu\beta)^{1/4} N^{-1/2} \sin^{-1/2}\alpha, \tag{2.6}$$

$$u_0 = (\nu\beta)^{-1/4} N^{-3/2} B_s \sin^{-1/2}\alpha, \tag{2.7}$$

$$b_0 = \nu^{1/4}\beta^{-3/4} N^{-1/2} B_s \sin^{-1/2}\alpha, \tag{2.8}$$

where $Pr \equiv \nu/\beta$ is the Prandtl number. A time scale $t_0 = l_0/u_0$ can also be defined from the above scales. Note that the above flow scales have different forms for the case with a constant buoyancy condition at the surface.

3. Linear stability analysis

Linearising (2.1)–(2.3) around Prandtl's laminar solution given by (2.4) and (2.5), and assuming that disturbances to the base flow given by Prandtl's solution are waves of the form $\boldsymbol{q}(x, y, z, t) = \hat{\boldsymbol{q}}(z) \exp\{\mathrm{i}(k_x x + k_y y) + \omega t\}$, the resulting equations have the form

$$\mathrm{i}k_x\hat{u} + \mathrm{i}k_y\hat{v} + \frac{\partial \hat{w}}{\partial z} = 0, \tag{3.1}$$

$$\omega\hat{u} + \mathrm{i}u_n k_x \hat{u} + u_n'\hat{w} = -\mathrm{i}k_x\hat{p} + \frac{Pr}{\Pi_s}\sin\alpha\left(-(k_x^2 + k_y^2)\hat{u} + \frac{\partial^2\hat{u}}{\partial z^2} + \hat{b}\right), \tag{3.2}$$

$$\omega\hat{v} + \mathrm{i}u_n k_x \hat{v} = -\mathrm{i}k_y\hat{p} + \frac{Pr}{\Pi_s}\sin\alpha\left(-(k_x^2 + k_y^2)\hat{v} + \frac{\partial^2\hat{v}}{\partial z^2}\right), \tag{3.3}$$

$$\omega\hat{w} + \mathrm{i}u_n k_x \hat{w} = -\frac{\partial\hat{p}}{\partial z} + \frac{Pr}{\Pi_s}\sin\alpha\left(-(k_x^2 + k_y^2)\hat{w} + \frac{\partial^2\hat{w}}{\partial z^2} + \hat{b}\cot\alpha\right), \tag{3.4}$$

$$\omega\hat{b} + \mathrm{i}u_n k_x \hat{b} + b_n'\hat{w} = \frac{\sin\alpha}{\Pi_s}\left(-(k_x^2 + k_y^2)\hat{b} + \frac{\partial^2\hat{b}}{\partial z^2} - (\hat{u} + \hat{w}\cot\alpha)\right), \tag{3.5}$$

where $\hat{u}$, $\hat{v}$, $\hat{w}$, $\hat{p}$, $\hat{b}$ are slope-normal-dependent flow disturbances normalised by the flow scales given in (2.6)–(2.8). k_x, k_y are real wavenumbers in the x (along-slope) and y (transverse) directions, respectively, whereas ω is a complex frequency. The normalised Prandtl base-flow solution and its derivative in the slope-normal direction in normalised coordinates are denoted by u_n, b_n and u_n', b_n', respectively. It can be seen from (2.4)–(2.5) that Prandtl's laminar velocity profile is a dampened sinusoidal oscillation, thus containing infinitely many inflection points, which opens the possibility of inviscid instabilities. From (3.1)–(3.5), it is clear that there are three dimensionless parameters characterising the idealised katabatic slope flow, which can also be confirmed independently by applying the Buckingham π theorem. These dimensionless parameters are: Prandtl number Pr, slope angle α, and a newly introduced stratification perturbation parameter Π_s, which is a measure of the ratio between the imposed surface buoyancy gradient and the background stratification. This unique parameter is determined from the externally imposed flow parameters as follows:

$$\Pi_s \equiv \frac{|B_s|\beta^{-1}}{N^2} = \frac{\left|\dfrac{\partial b}{\partial z}(0)\right|}{N^2}. \tag{3.6}$$

Since the buoyancy flux at the surface, B_s, is negative for katabatic slope flows and positive for anabatic slope flows, the magnitude of B_s is used in the definition of Π_s. The slope flow is expected to become dynamically more unstable at higher Π_s. Note that Π_s can also be related to the so-called internal Froude number as $\Pi_s = Fr\sqrt{Pr}$, and to the bulk Richardson number as $\Pi_s = \sqrt{Pr/Ri}$. In relating Π_s to Ri and Fr, we have used the internal length and velocity scales defined in (2.6) and (2.7), respectively. However, use of Fr or Ri are not preferred for the current flow problem because there are no externally imposed velocity or length scales.

It is important to mention that Π_s shares common terms with the flow forcing parameter, $Fp_B \equiv B_s\nu^{-1}/N^2$, that was introduced in Fedorovich & Shapiro (2009). The apparent difference between these two dimensionless parameters is that thermal diffusivity, β, is used in Π_s, whereas kinematic viscosity, ν, is used in Fp_B. The physical interpretations of these dimensionless parameters are different. Fedorovich & Shapiro interpreted Fp_B as the ratio between the energy production at the surface and the work against buoyancy as well as viscous forces. In our proposition, we interpret Π_s as the degree of disturbance to the background stable stratification by heat conduction at the surface, which is also evident by the appearance of Π_s in (3.5). These two dimensionless parameters are related to each other through the Prandtl number as $\Pi_s = PrFp_B$. As we show later in § 3.3, stability characteristics of slope flows depend strongly on the Prandtl number. Therefore, in our view, Fp_B and Π_s are distinct dimensionless parameters with unique interpretations.

The linearised equations can be written as a generalised eigenvalue problem as follows:

$$A(k_x, k_y)\hat{\boldsymbol{q}}(z) = \omega \boldsymbol{M}\hat{\boldsymbol{q}}(z), \tag{3.7}$$

where $\hat{\boldsymbol{q}}(z) = [\hat{u}(z), \hat{v}(z), \hat{w}(z), \hat{p}(z), \hat{b}(z)]^{\mathrm{T}}$ is the vector of flow disturbances varying in the slope-normal direction. $\boldsymbol{M}$ is a singular matrix arising from the primitive variable formulation; it is created from the identity matrix by setting all diagonal entries belonging to the continuity equation to zero. The appropriate boundary conditions for this problem are no-slip for disturbance velocities at $z = 0$, free slip at $z \to \infty$, and for buoyancy disturbance $\partial\hat{b}/\partial z|_0 = 0$, $\hat{b}|_{z\to\infty} = 0$ are imposed. The pressure disturbance $\hat{p}$ is also set to zero at both $z = 0$ and $z \to \infty$. The generalised eigenvalue problem (3.7) is solved via a collocated spectral method using Chebychev polynomials and an algebraic map to cover the semi-infinite domain $[0, \infty)$. Two hundred collocation points are used for discretisation, and the resulting generalised eigenvalue problem is solved with the help of the `eigs` function in MATLAB. Linear stability of the problem is associated with the real part of the eigenvalues ω, where $\mathrm{Re}\{\omega\} > 0$ represents a positive exponential growth for the corresponding eigenmode, thus an unstable mode. The imaginary part of ω is the temporal oscillation frequency for the corresponding eigenmode, and $\mathrm{Im}\{\omega\} = 0$ represents a stationary mode.

3.1. *Linear growth rates*

To explore the linear instability mechanism dependent on the longitudinal and transverse wavenumbers, the maximal real value of the spectrum for a range of normalised wavenumber vectors (k_x, k_y) is calculated at various fixed values of α and Π_s. Since our interest is in katabatic winds we assume $Pr = 0.71$, which is a suitable value for air at approximately 2 °C. For a slope angle of $\alpha = 3^\circ$ and $\Pi_s = 1.66$, the maximal possible growth rates for wavenumber vectors $[k_x, k_y]$ within the interval $[0, 0.065] \times [0, 0.5]$ are shown in figure 2(*a*). Only the positive growth rates, i.e. unstable modes, are highlighted. It can be seen that the growth rates tend to grow with decreasing k_x component such that the maximal instabilities occur at $k_x = 0$, i.e. the most unstable modes are purely along the direction transverse to the base-flow direction; the transverse wavenumber at which maximal possible growth rate is attained is valued at approximately $k_y \approx 0.33$, as evident from an inspection of the k_y-axis of figure 2(*a*). The imaginary part of the eigenvalues corresponding to the maximal positive growth rates are all zero, which indicates that the transverse instabilities studied here are all stationary vortex rolls. This behaviour is in stark contrast to other parallel flows such as the plane Poiseuille flow, for which Squire's theorem stipulates that the most unstable mode propagates parallel to the direction

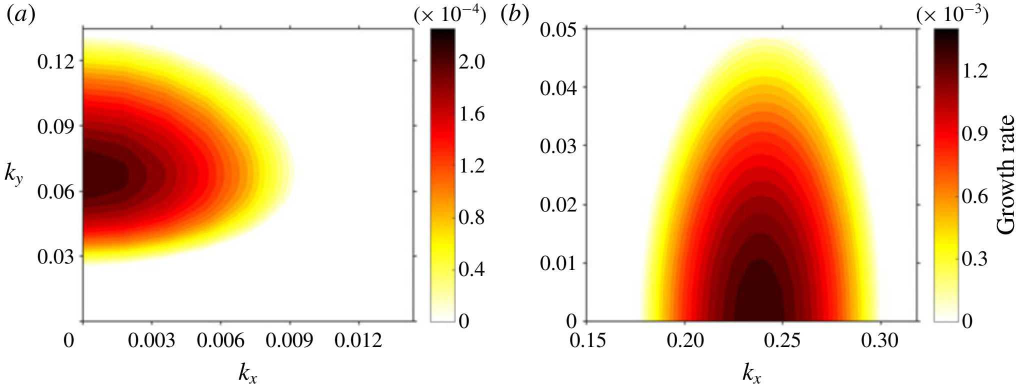

FIGURE 2. Growth rate contours depending on wavenumber vectors k_x, k_y for $Pr = 0.71$. (*a*) $\alpha = 3^\circ$, $\Pi_s = 1.6$; (*b*) $\alpha = 66^\circ$, $\Pi_s = 18.5$.

of the base flow (Schmid & Henningson 2001). Thus, it could be inferred that the negative buoyancy force acting simultaneously orthogonal as well as parallel to the base-flow direction is responsible for the transverse mode of instability, which is analogous to the role centrifugal force plays in other types of similar instabilities, such as Görtler vortices or vortices appearing in Taylor–Couette flow (Taylor 1923; Schmid & Henningson 2001). For instance, in an earlier work by Görtler (1959), the normal buoyancy force as well as surface curvature have both been identified as key ingredients for the creation of longitudinal vortices on a curved, cooled surface. From the results of our work, it can be seen that even in the presence of stable stratification with strength N^2, if the buoyancy force due to surface cooling is sufficiently strong, as measured by the perturbation parameter Π_s, then the aforementioned instability mechanism inherent in the unstratified cases will be able to overcome the stable background stratification.

At the steep slope angle of $\alpha = 66^\circ$ and with a higher stratification perturbation number of $\Pi_s = 18.5$, the maximal possible growth rates for wavenumber vectors $[k_x, k_y]$ within the interval $[0.15, 0.33] \times [0, 0.05]$ are displayed in figure 2(*b*). In contrast to the situation at $\alpha = 3^\circ$, figure 2(*b*) shows that the growth rates tend to increase with decreasing k_y component such that the maximal instabilities occur at $k_y = 0$; the longitudinal wavenumber at which maximal possible growth rate is attained is valued at approximately $k_x \approx 0.24$, as evident from figure 2(*b*). The most unstable mode are hence purely along the slope direction, parallel to the base-flow direction. This behaviour agrees with instability in other types of parallel flow such as plane Poiseuille flow or Rayleigh–Benard convection. This major deviation from the behaviour of slope flows at the moderate slope angle of $\alpha = 3^\circ$ could be attributed to the stronger longitudinal gravity component which dominates the stable stratification orthogonal to it at steeper slope angles. Another difference from the moderate slope case (i.e. $\alpha = 3^\circ$) is that the imaginary part, i.e. normalised oscillation frequency of the most unstable mode, is approximately 0.115. Thus, in contrast to the transverse instability at moderate slope angles, the longitudinal instability on steep slopes is non-stationary. In both the moderate as well as the steep slope configurations, however, the most unstable instability mode propagates either parallel ($k_y = 0$) or orthogonal ($k_x = 0$) to the along-slope direction, but never in an oblique direction($k_x, k_y \neq 0$), which is a different behaviour than oblique instabilities observed in the spanwise-stratified Couette flow studied by Facchini *et al.* (2018).

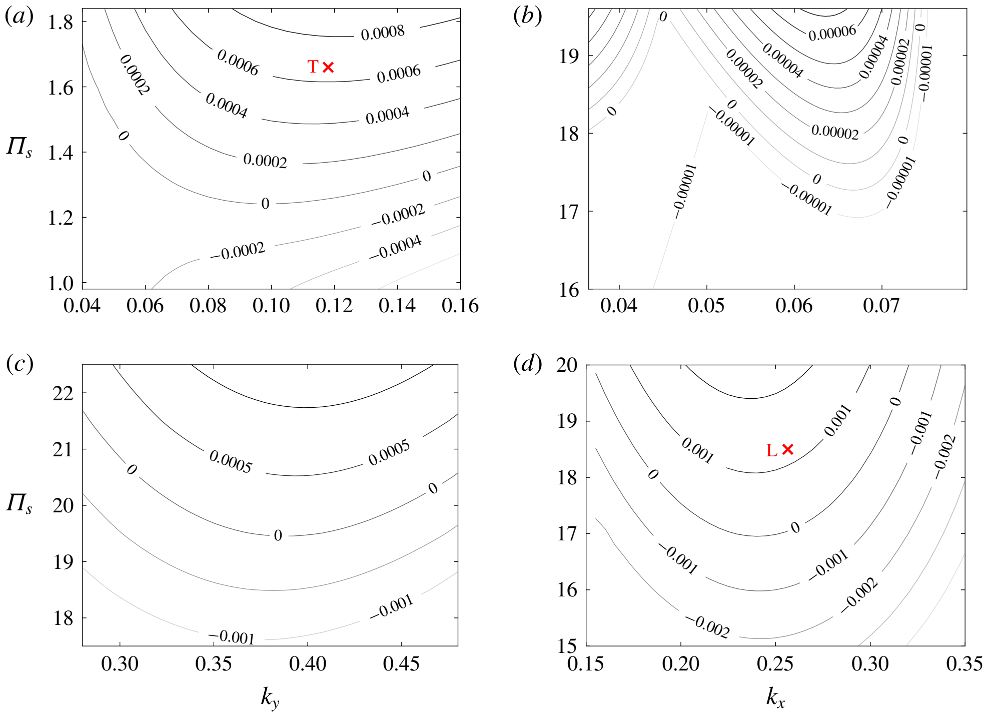

FIGURE 3. Growth rate contours at $\alpha = 3^\circ$ for (*a*) transverse and (*b*) longitudinal modes and at $\alpha = 66^\circ$ for (*c*) longitudinal and (*d*) transverse modes. The most unstable eigenvalue ($\omega \approx 6.6 \times 10^{-4}$) for the transverse mode with $k_y = 0.12$ is highlighted with the marker T in (*a*). The most unstable eigenvalue ($\omega \approx 0.0013 + 0.115i$) for the longitudinal mode with $k_x = 0.25$ is highlighted with the marker L in (*d*). DNS are performed for these two marked cases in § 4.

3.2. *Neutral curves and critical stability*

The results from the previous subsection support the assertion that the most unstable modes at each slope angle α and stratification perturbation Π_s are propagating along either the base-flow direction or the transverse direction, i.e. only one component of the wavenumber vector $[k_x, k_y]$ is non-zero in order to attain maximal growth rates. Based on this discovery, the critical Π_s for the onset of instability at a specific slope angle α and Pr number can be found by plotting the growth rate contours over a range of Π_s separately for k_x and k_y, assuming that the other wavenumber is zero, respectively. In the following, a constant $Pr = 0.71$ is assumed. For $\alpha = 3^\circ$, the results are shown in figure 3(*a,b*). It can be seen that the minimal Π_s for the transverse mode is approximately 5, whereas the longitudinal mode requires a minimal $\Pi_s = 15.3$ to become unstable. Thus, the most dominant instability in this case is the transverse mode, in agreement with growth rate analysis of the previous subsection (see figure 2*a*). In figure 3(*c,d*), the results for a steep angle of $\alpha = 66^\circ$ are displayed. This time, it can be observed that the minimal Π_s for the longitudinal mode is approximately 17, whereas the transverse mode requires a minimal $\Pi_s \approx 19.5$ to become unstable. This means that in contrast to the case of shallower slope angle, the instability to be triggered first at $\alpha = 66^\circ$ extends along the slope direction parallel to the base flow, which is also supported by the previous growth rate analysis and

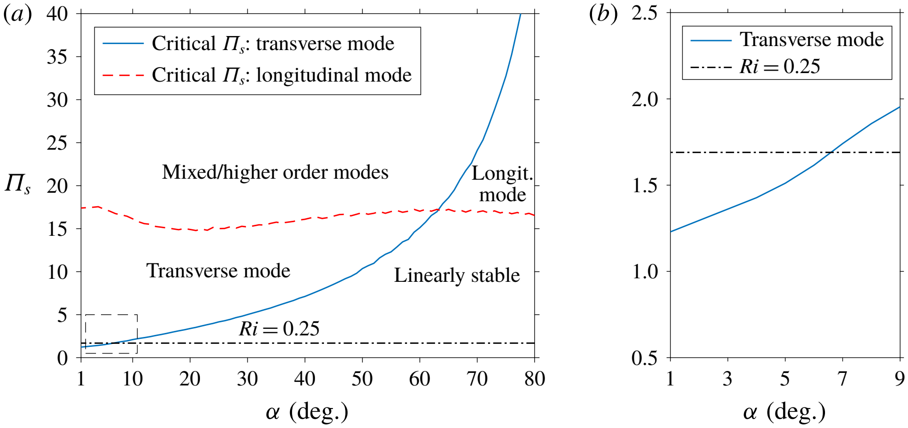

FIGURE 4. (*a*) $\varPi_s - \alpha$ instability map for katabatic slope flows at $Pr = 0.71$. The labels delineate regions in the $(\varPi_s, \alpha)$ parameter space within which a particular type of instability is dominant. (*b*) Zoomed view of the low-angle region in the stability map where instability occurs for $\varPi_s$ values with implied $Ri > 0.25$.

figure 2(*b*). In all cases, it can be observed from figure 3 that the unstable growth rates increase with increasing $\varPi_s$, hence pointing to general instability at $\varPi_s \rightarrow \infty$ or $\nu \rightarrow 0$. This implies that the instability mechanism must be caused by an inviscid mechanism due to the oscillatory profile of Prandtl's laminar solution.

3.3. *Dependence on the slope angle and the Prandtl number*

The previous subsections have demonstrated a drastic change in the nature of the flow instability with increasing slope angle, characterised by a switch from the transverse to the longitudinal direction at sufficiently steep angle due to the increasing longitudinal gravity component driving the flow. To further explore the influence of slope angle, α, on the instability, the critical stability threshold of $\varPi_s$ for both longitudinal and transverse instabilities as functions of α over the interval $[5^\circ, 80^\circ]$ are determined and displayed in figure 4(*a*). It can be clearly observed that while the critical stratification perturbation parameter, $\varPi_s$, for the transverse instability is lower at shallow angles, it increases for increasing α, and the critical value for the longitudinal instability stays almost constant over the same range of slope angles. This means that the transverse mode becomes increasingly stable with growing α, and the angle at which its critical threshold value of $\varPi_s$ equals that of the longitudinal mode is approximately $\alpha \approx 62^\circ$. From the relation $\varPi_s = \sqrt{Pr/Ri}$ given in § 3, the $\varPi_s$ value that corresponds to a Richardson number of 0.25 at $Pr = 0.7$ is $\varPi_s \approx 1.69$ and is represented by the horizontal line in figure 4(*a*). The region above this line implies $Ri < 0.25$, and it can be seen from figure 4(*a*) that for steep slope angles $\alpha > 62^\circ$ the critical value of $\varPi_s$ for either instability mode is at least 17, and hence linearly stability holds for Ri as low as 2.5×10^{-3}.

The effect of the Prandtl number on the stability diagram for the two different modes are displayed in figure 5, which shows the minimal $\varPi_s$ needed to trigger instability depending on the slope angle. It can be seen that for both transverse and longitudinal modes, an increase in Pr tends to raise the critical $\varPi_s$ threshold required for instability. This is readily explained by the fact that when all other

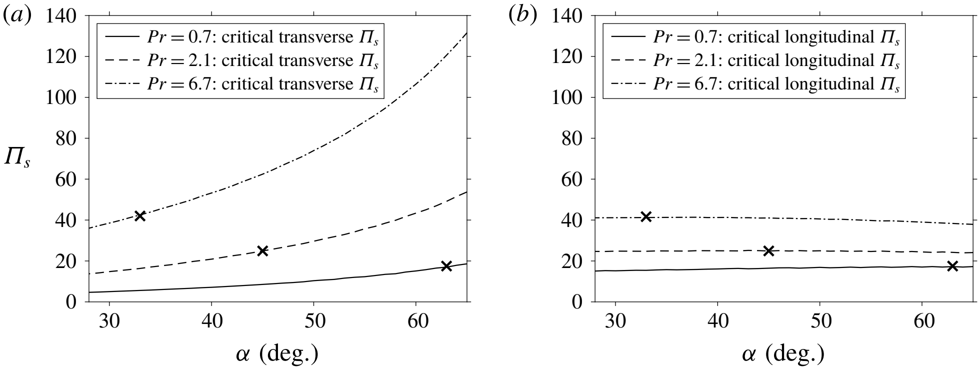

FIGURE 5. Prandtl number dependence of the critical Π_s values for the transverse mode (*a*) and the longitudinal mode (*b*) of instability. The marker (×) highlights the transition point from one mode to the other.

parameters in the flow configuration are held constant, a larger Pr corresponds to a lower thermal diffusivity, β, which implies a smaller surface heat flux B_s at the same surface buoyancy gradient and Π_s, as evidenced by (3.6). The curves on figure 5(*a,b*) also demonstrate that the stability threshold for the transverse mode is affected much more strongly by Pr than the longitudinal mode; indeed, by increasing Pr from the value of 0.7 for air to 6.7 for water at room temperature, the critical Π_s of the transverse mode becomes more than six times larger for nearly all angles, whereas for the longitudinal mode the critical Π_s only assume values approximately twice as high as for the low-Pr case.

3.3.1. *Stability behaviour at small slope angles*

From figure 4(*a*), it can be seen that for slope angles with $\alpha < 20^\circ$, the critical Π_s for the transverse mode, in contrast to the longitudinal mode, continues to decrease with smaller angle, such that at $\alpha = 5^\circ$ the critical value is $\Pi_s \approx 1.61$. A closer look of the stability curve for small angles is shown in figure 4(*b*). Since Π_s is related to the Richardson number via $Ri = Pr/\Pi_s^2$, it follows that for slope angles $\alpha \leqslant 5^\circ$, the Prandtl base flow satisfies $Ri > 0.25$ throughout, thus apparently not meeting the stability criterion stipulated by the Miles–Howard theorem for parallel base flows under stably stratified conditions (e.g. Drazin & Reid 2004). Hence, shallow-angle Prandtl slope flows serve as an example of a parallel base flow that exhibits a transverse mode of instability with Richardson number larger than 0.25 throughout. However, the Miles–Howard theorem, as formulated by Miles (1961), is based on the assumption of inviscid free flow without buoyancy force acting along the base-flow direction; it also ignores viscous shear as well as heat conduction. Candelier *et al.* (2011) have demonstrated that when shear is not aligned with stratification, a stably stratified, inviscid flow can be unstable while $Ri > 0.25$ holds within the entire flow. As shown by Miller & Gage (1972), the presence of viscous shear can also destabilise a parallel flow under stable stratification despite satisfying $Ri > 0.25$ throughout. Thus, we can conclude that viscous and heat conduction effects as well as misalignment of shear and stratification contribute towards the formation of the transverse mode of instability at $Ri > 0.25$ displayed in figure 4(*b*).

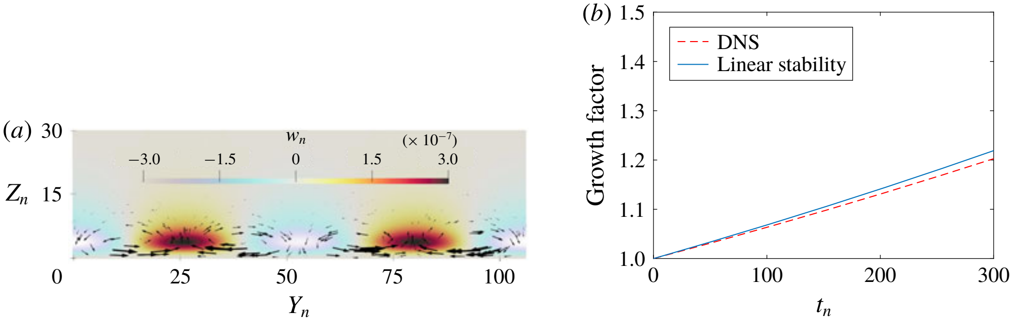

FIGURE 6. Transverse mode at $\alpha = 3°$, $\Pi_s = 1.66$: (*a*) disturbance flow vector field and normalised slope-normal velocity w_n on the y–z plane. Slope flow is into the page; (*b*) temporal growth.

4. Direct numerical simulations

We carry out direct numerical simulations (DNS) to independently validate the findings from the linear stability analysis and visualise flow structures induced by flow instabilities. We solve the buoyancy-driven incompressible flow equations (2.1)–(2.3) using a Cartesian mesh three-dimensional Navier–Stokes solver (Jacobsen & Senocak 2013). The code adopts a second-order accurate Adams–Bashforth scheme for time advancement and second-order central difference scheme for spatial derivatives. The pressure Poisson equation is solved with a geometric multigrid technique. Umphrey *et al.* (2017) validated the current code using the Prandtl model and demonstrated globally second-order accurate solutions. The simulation domains are rectangular boxes of dimensional size $L_x \times L_y \times L_z$. The mesh resolution is such that there are at least four points per characteristic length scale l_0 along each direction in all simulated cases except for the last one, which will be described separately. Periodic boundary conditions are imposed in both the longitudinal and transverse directions, whereas no-slip conditions with a constant buoyancy flux are applied on the lower surface at $z = 0$, and the top surface is subject to an adiabatic free-slip condition. The top boundary was placed at least 50 times the characteristic slope length scale l_0 given by (2.6) above the surface to capture quiescent conditions aloft. The longitudinal and transverse size of the domain are chosen to be an integer multiple of the targeted wavelength of an instability in the particular direction. The initial conditions for velocity and buoyancy are Prandtl's laminar solution (2.4)–(2.5) without any explicitly added disturbances. Roundoff errors due to massively threaded double-precision floating point computations on graphics processing units and arising from interpolation of the Prandtl base solution onto the finite numerical grid as well as due to the iterative nature of computations were sufficient to trigger instabilities predicted by the linear theory.

4.1. *Transverse mode of instability*

For the case with $\alpha = 3°$, $\Pi_s = 1.66$ and $Pr = 0.71$, a DNS is carried out over a domain with size $50l_0 \times 106l_0 \times 50l_0$, where l_0 is the length scale defined in (2.6). The results confirm a stationary purely transverse instability, agreeing with the LSA and growth rate analysis in § 3.1. In figure 6(*a*), the instantaneous velocity disturbance profile projected onto a plane normal to the main velocity is shown. It can be seen that the

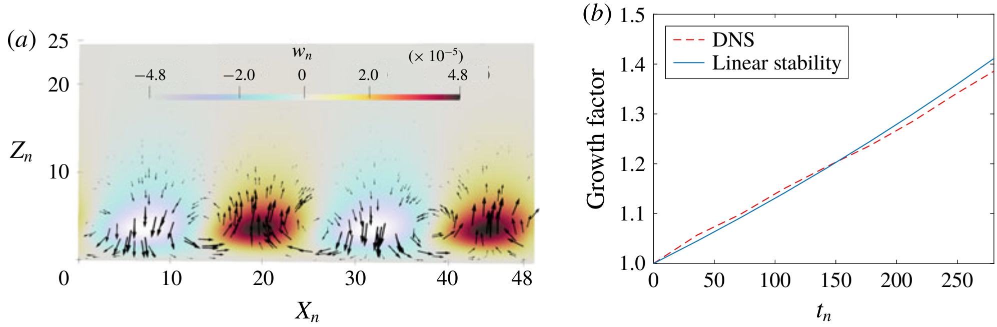

FIGURE 7. Longitudinal mode at $\alpha = 66^\circ$, $\Pi_s = 18.5$. (*a*) Disturbance flow-field vector and normalised slope-normal velocity w_n on the x–z plane. Slope flow is from right to left; (*b*) temporal growth.

normalised wavelength of the simulated instability is approximately $\lambda_n = \lambda_y/l_0 \approx 18$, corresponding to a normalised wave vector of $k_y = 2\pi/\lambda_n \approx 0.35$. To measure the temporal growth of the instability, the growth factor $G(t) = \sqrt{\langle w^2\rangle(t)}/\sqrt{\langle w^2\rangle(t_0)}$ for $t > t_0$ is introduced, defined as the spatial root-mean-squared vertical velocity normalised by the value at reference time t_0. The simulated temporal growth of the instability is plotted alongside the growth rate predicted by linear stability theory for $k_y = 0.35$, $\Pi_s = 1.66$, as marked by point T in figure 3(*a*), which also corresponds to $[0, k_y]$ in figure 2(*a*). The non-dimensional growth rate from the DNS has a value of approximately 6.15×10^{-4}, closely agreeing with the value of 6.66×10^{-4} predicted via the linear stability theory.

4.2. *Longitudinal mode of instability*

For the case with the slope angle $\alpha = 66^\circ$, $\Pi_s = 18.5$ and $Pr = 0.71$, a DNS is conducted on a domain with dimensions $50l_0 \times 25l_0 \times 50l_0$. In agreement with the analysis in § 3.1, the simulation results show an oscillating instability propagating along the slope direction. Figure 7(*a*) displays the instantaneous disturbance velocity profile on a plane parallel to the base-flow direction and normal to the surface. It can be seen that the normalised wavelength of the simulated instability is approximately $\lambda_n = \lambda_x/l_0 \approx 25$, corresponding to a normalised wave vector of $k_x = 2\pi/\lambda_n \approx 0.25$. The temporal growth of the instability is tracked by the same growth factor $G(t)$ used for the analysis of transverse instability. The simulated temporal growth of the instability is shown with the growth curve resulting from linear stability theory in figure 7(*b*). The non-dimensional growth rate from the simulation has a value of approximately 1.2×10^{-3}, in close agreement with the prediction from LSA for $k_x = 0.25$, $\Pi_s = 18.5$, highlighted with the marker L in figure 3(*d*), also visible as $[k_x, 0]$ on figure 2(*b*). According to LSA, the normalised frequency of the longitudinal instability for this particular set of parameters is approximately 0.115. The simulated instability has a normalised frequency of 0.125, which is close to the LSA results.

4.3. *Mixed mode of instability*

For the case with $\alpha = 66^\circ$ as discussed previously, if the flow is subjected to more unstable conditions, i.e. Π_s is further increased beyond 20, then according

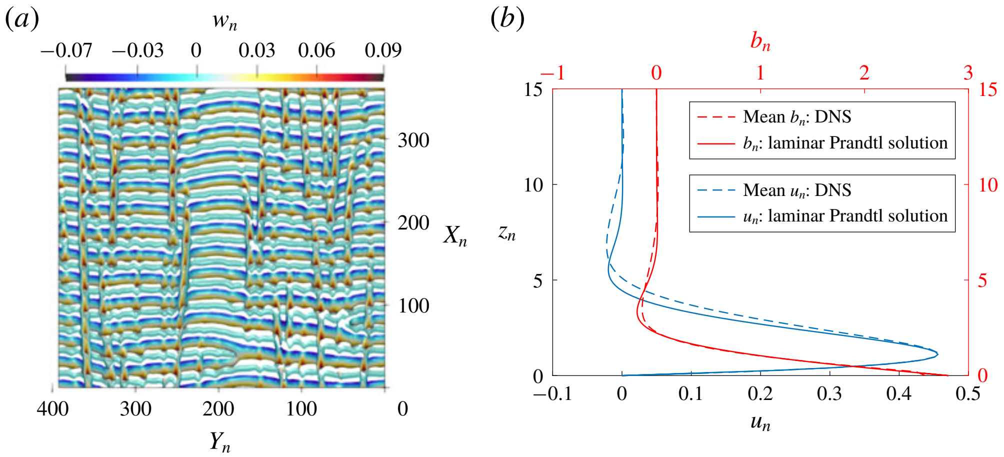

FIGURE 8. Mixed-mode instability at $\alpha = 66^\circ$, $\Pi_s = 25$. (*a*) Q-criterion contour visualisation of the instantaneous vorticity field, coloured by the normalised slope-normal velocity w_n; (*b*) comparison of the normalised mean velocity and buoyancy profiles against the Prandtl solution.

to figure 4, both the transverse and longitudinal modes will become unstable. For subsequent discussions, Π_s is fixed at 25. Simulation for this case is carried out on a comparatively larger domain of $400l_0 \times 400l_0 \times 50l_0$ to capture multiple vortex rolls along all directions. Since, in this case, the horizontal dimensions of the simulation domain are an order of magnitude larger than the height, a less refined grid resolution is chosen for the along-slope and cross-slope directions than in the two previous cases such that there are approximately two grid points per length scale l_0 along these directions. An instantaneous snapshot of the full flow field is shown in figure 8(*a*). Here, the isocontour of the Q-criterion at 4 % of its maximal positive value is used for vortex identification (cf. Kolář 2007). Both longitudinal and transverse vorticity rolls are simultaneously present in the flow field, and are intricately interwoven with each other.

Figure 8(*b*) compares the spatiotemporally averaged velocity and buoyancy profiles from the simulated unstable flow field with the Prandtl's solution with the same laminar flow parameters. The total averaging time window is roughly 30 times the flow-through-time based on the mean velocity at the jet tip. The comparison shows that at low altitudes, there is very little difference between the averaged unstable profile and the laminar Prandtl profile. At higher altitudes above the jet, however, the flow pattern is visibly altered; the mean velocity magnitude of the unstable flow decays more slowly with growing height than the laminar solution due to enhanced mixing caused by the instability. On the other hand, modification of the mean buoyancy field from the Prandtl profile is much weaker. As evident from the lack of small scales in figure 8(*a*), the flow is not turbulent but the mixed-mode instability is already influential in modifying Prandtl's laminar velocity profile noticeably.

5. Conclusions

Despite its apparent simplicity, Prandtl's katabatic slope flow model exhibits a surprisingly rich structure in linear response to small perturbations. It is prone to distinct instabilities governed by three dimensionless parameters, which are the Prandtl number, the slope angle, and a stratification perturbation parameter, Π_s, that we have introduced in the present work. For low to moderate slope angles, a three-dimensional, stationary transverse mode of instability is predicted to develop, even though Prandtl's profile is a parallel flow; for steep slopes beyond 62°, an oscillatory longitudinal instability is triggered instead due to the growing gravity component along the slope direction. At sufficiently small angles such that $\alpha \lesssim 5^{\circ}$, the transverse mode of instability can develop under conditions with implied Richardson number exceeding the critical value of 0.25 as stipulated by the Miles–Howard theorem. Thus, the Prandtl model for shallow slopes is an example of a parallel flow that does not satisfy the well-known $Ri > 0.25$ condition for stability. The disagreement with the Miles–Howard theorem can be explained by the presence of viscous and heat conduction effects as well as misalignment of shear with stratification. For sufficiently high values of Π_s, both instabilities coexist, leading to an intricate pattern of crisscrossing vortex rolls.

An important implication of our current study is that, for a given fluid, linear stability of katabatic slope flows cannot simply be determined by a single dimensionless parameter alone, such as the Richardson number. Indeed, recently, a growing number of results have emerged to show that a single Ri-criterion given by the Miles–Howard theorem is inadequate to reliably predict the onset of instability in stably stratified flows (e.g. Miller & Gage 1972; Candelier *et al.* 2011; Kaminski, Caulfield & Taylor 2017). Our study adds to this existing pile of evidence by demonstrating that in the case of katabatic slope flows, slope inclination, background stratification as well as heat transfer rate at the surface are all important parameters governing the stability of the given flow configuration. Future prospective modelling and parameterisations of stably stratified flows on complex surfaces may benefit from considering this non-trivial dependence in their formulations.

Acknowledgements

Research was sponsored by the Army Research Office and was accomplished under Grant no. W911NF-17-1-0564 with Dr J. G. Baryzk as the programme manager. This research was supported in part by the University of Pittsburgh Center for Research Computing through the resources provided.

References

Candelier, J., Le Dizès, S. & Millet, C. 2011 Shear instability in a stratified fluid when shear and stratification are not aligned. *J. Fluid Mech.* **685**, 191–201.

Chen, J., Bai, Y. & Le Dizès, S. 2016 Instability of a boundary layer flow on a vertical wall in a stably stratified fluid. *J. Fluid Mech.* **795**, 262–277.

Drazin, P. G. & Reid, W. H. 2004 *Hydrodynamic Stability*, 2nd edn. Cambridge University Press.

Facchini, G., Favier, B., Le Gal, P., Wang, M. & Le Bars, M. 2018 The linear instability of the stratified plane Couette flow. *J. Fluid Mech.* **853**, 205–234.

Fedorovich, E. & Shapiro, A. 2009 Structure of numerically simulated katabatic and anabatic flows along steep slopes. *Acta Geophys.* **57** (4), 981–1010.

Görtler, H. 1959 Über eine Analogie zwischen den Instabilitäten laminarer Grenzschichtströmungen an konkaven Wänden und an erwärmten Wänden. *Ing.-Arch.* **28** (1), 71–78.

Jacobsen, D. A. & Senocak, I. 2013 Multi-level parallelism for incompressible flow computations on GPU clusters. *Parallel Comput.* **39** (1), 1–20.

Kaminski, A. K., Caulfield, C. P. & Taylor, J. R. 2017 Nonlinear evolution of linear optimal perturbations of strongly stratified shear layers. *J. Fluid Mech.* **825**, 213–244.

KOLÁŘ, V. 2007 Vortex identification: new requirements and limitations. *Intl J. Heat Fluid Flow* **28** (4), 638–652.

MILES, J. W. 1961 On the stability of heterogeneous shear flows. *J. Fluid Mech.* **10** (4), 496–508.

MILLER, J. R. & GAGE, K. S. 1972 Prandtl number dependence of the stability of a stratified free shear layer. *Phys. Fluids* **15** (5), 723–725.

PRANDTL, L. 1942 *Führer durch die Strömungslehre*. Vieweg und Sohn.

SCHMID, P. J. & HENNINGSON, D. S. 2001 *Stability and Transition in Shear Flows*. Springer.

SHAPIRO, A. & FEDOROVICH, E. 2004 Unsteady convectively driven flow along a vertical plate immersed in a stably stratified fluid. *J. Fluid Mech.* **498**, 333–352.

SHAPIRO, A. & FEDOROVICH, E. 2014 A boundary-layer scaling for turbulent katabatic flow. *Boundary-Layer Meteorol.* **153** (1), 1–17.

TAYLOR, G. I. 1923 Stability of a viscous liquid contained between two rotating cylinders. *Phil. Trans. R. Soc. Lond.* A **223** (605–615), 289–343.

UMPHREY, C., DELEON, R. & SENOCAK, I. 2017 Direct numerical simulation of turbulent katabatic slope flows with an immersed boundary method. *Boundary-Layer Meteorol.* **164** (3), 367–382.